

1
2
3
4
5
6
7
8
9
10
11
12
13
14
15
16
17
18
19
20
21
22
23
24
25
26
27
28
29
30
31
32
33
34
35
36
37
38
39
40
41
42
43
44
45
46
47
48
49
50
51
52
53
54
55
56
57
58
59
60
61
62
63
64
65

On the use of the Radon transform to estimate longshore currents from video imagery

Rafael Almar^{1,*}, Stanislas Larnier², Bruno Castelle³, Timothy Scott⁴, France
Floc'h⁵

Abstract

A direct estimation of longshore currents using in-situ instruments is difficult and costly, and often limited to punctual measurements over short durations. Video remote sensing systems offers an alternative when drifting features, like foam induced by breaking waves or other streaks, are visible. In this paper we describe a method based on the application of the Radon transform on longshore spatio-temporal images. The sinogram from the Radon transform is used to find the angle of the drifting, further converted into current. Our approach is first tested using synthetic fields created using anisotropic Gaussian random currents and waves. Comparison is also made with in-situ currents from the Grand Popo 2014 experiment in Benin (Gulf of Guinea, West Africa). Results show an overall good agreement ($O(30\%)$) in the swash, surf and inner shelf zones while the method offers best skills in the surf zone (17%) where the drifting foam induced by wave breaking is evident. The width of the Radon peak is found to be a good proxy of accuracy. This remote sensing method allows a long term monitoring of the longshore current and its cross-shore structure, which brings new perspectives in quantifying sediment drift variability.

Keywords: Nearshore, Video imagery, anisotropic Gaussian random fields,

*Corresponding author

Email address: rafael.almar@ird.fr (Rafael Almar)

¹IRD-LEGOS (CNRS/Univ. Toulouse/IRD/CNES), Toulouse, France

²CNRS-LAAS, Toulouse, France

³EPOC (CNRS/Univ. Bordeaux), Bordeaux, France

⁴University of Plymouth, UK

⁵LDO-IUEM, Brest, France

1. Introduction

Longshore current has attracted a major attention in the nearshore science for decades, generally within the scope of estimating longshore sediment transport (Komar, 1998). It is generated by oblique breaking waves, is rather vertically uniform and can reach values up to meter per second (Komar & Inman, 1970; Lippmann, 1970). Observations have shown that longshore current peaks at the location of the maximum of breaking and can present a multi-modal structure in case of barred beach (Schoonees & Theron, 1993; Putrevu & Svendsen, 1995; Haller & Svendsen, 2002; Feddersen, 2014). Tidal modulation of wave breaking and subsequent longshore current can be large, in particular at low tide terrace and barred beaches (Thornton & Guza, 1986; Feddersen, 2003), and intense current (> 0.5 m/s) have shown to present a substantial variability at low frequency scales (minutes), likely explained by shear instabilities (Allen et al., 1996; Oltman-Shay et al., 1989). At longer term, seasonal to inter-annual fluctuations are likely to be induced by wave conditions modulation due to climatic modes (Splinter et al., 2012; Almar et al., 2015). Suited documentation on its multi-scale spatio-temporal evolution has long been hampered by difficulties in measuring such fluctuating structures by conventional in-situ instrument arrays, while the application of recent shore-based remote sensing methods has a large potential.

Radars and video imagery have proved to be very efficient tools in monitoring the nearshore and in particular the surface current (Holman & Haller, 2013), for a reasonable running cost and over typical areas of kilometers and footprint of meters. Radar-based Doppler effect of backscattered signal from rough surface (Haller & Svendsen, 2014) is probably the most direct way in estimating surface currents. Video systems have been developed for over twenty years (Holman & Haller, 2013). From their incomparable low cost (< 1000 eur) and intuitive use, video stations are rapidly growing over world coasts, including developing coun-

1
2
3
4
5
6
7
8
9 29 tries, offering the exciting potential of an unequaled documentation of coastal
10 30 zones from local to regional scale (Mole et al., 2013). Video methods were ap-
11 31 plied originally to estimate submerged and intertidal bathymetry (Lippmann
12 32 & Holman, 1990; Stockdon & Holman, 2000) and time-varying location of the
13 33 shoreline (Plant & Holman, 1997). Following the improvement of sensors resolu-
14 34 tion, an increasing number of methods have been developed recently to quantify
15 35 wave’s characteristics (Lippmann & Holman, 1991; De Vries et al., 2011; Stock-
16 36 don & Holman, 2000; Almar et al., 2012) but only a few were dedicated to
17 37 surface currents (Holman & Haller, 2013), though its key importance.

18 38 In this paper, we are interested in estimating the longshore current from
19 39 video, in a similar way to (Chickadel et al., 2003). This contrasts with the two-
20 40 dimensional approach based on a Particle Image Velocimetry (PIV) method
21 41 (Holland et al., 2001; Puloe et al., 2003) generally applied in laboratory experi-
22 42 ments (Cox & Anderson, 2001; Kimmoun & Branger, 2007) because it requires
23 43 high temporal and spatial resolutions. Our choice of a one-dimensional ap-
24 44 proach rises from the availability of video spatio-temporal images (also called
25 45 Hovmoller diagram or timestack) widely used to conserve high frequency infor-
26 46 mation of cross-shore and longshore waves and current components, avoiding
27 47 saving the whole high frequency video, which is particularly pertinent for long
28 48 term monitoring. The second interest is because spatio-temporal format is per-
29 49 fectly suited for angle separation methods based on the Radon transform (RT,
30 50 (Radon, 1917)). The RT has recently been successfully applied to ocean waves,
31 51 in particular for the detection of ship wave (Copeland et al., 1995) and more
32 52 recently to nearshore wave dynamics (Yoo et al., 2011; Almar et al., 2014a)
33 53 and swash (Yoo et al., 2009) but no attempt was conducted to estimate the
34 54 longshore current, despite the high potential of use.

35 55 In the next section our method is tested over synthetic data and field observa-
36 56 tion from Grand Popo, Benin (Gulf of Guinea, West Africa). The Bight of Benin
37 57 is subject to increasing erosion due to anthropic perturbation of the strong long-
38 58 shore sediment transport (approximately $500.000 \text{ m}^3/\text{yr}$, (Almar et al., 2015))
39 59 exacerbated by the rapid development of deep water harbors in the main cities

1
2
3
4
5
6
7
8
9
60 from Accra to Lagos. Observing and quantifying this longshore drift is crucial
10 here to improve coastal zone management. The RT algorithm is described in
11 the first section and the synthetic and field datasets used in this paper are pre-
12 sented in the second section. In third section, the method's skills are tested
13 against these synthetic and field data, an application is provided to illustrate
14 the potential of the method and finally some concluding remarks are given.
15
16
17
18
19

20 **2. Radon transform and algorithm**

21 *2.1. Radon transform*

22
23
24 The Radon transform (Ramm & Katsevich, 1996; Mallat, 2008; Feeman,
25 2010) $R(\rho, \theta)$ over a bi-dimensional field $\mu(x, y)$ can be defined as:
26

$$27 \quad R(\rho, \theta) = \iint \mu(x, y) \delta(x \cos(\theta) + y \sin(\theta) - \rho) dx dy \quad (1)$$

28
29
30 where δ is the Dirac delta function, θ and ρ are respectively the angle and
31 distance from origin of the integration line defined as $\rho = x \cos(\theta) + y \sin(\theta)$.
32 The origin is the center of the two-dimension field. The Radon transform $R(\rho, \theta)$
33 is defined for all possible values of θ from $[0 \text{ to } 180^\circ]$ and ρ from 0 to the diagonal
34 length.
35
36
37
38

39 [Figure 1 about here.]
40

41 The Figure 1 shows the application of the RT to a disk and inclined lines.
42 The projection of a disk in Figure 1.a has a constant density at all angles while
43 the projection of the lines in Figure 1.d has two peaks, indicating their angles
44 θ .
45
46
47

48 [Figure 2 about here.]
49

50 *2.2. Orientation detection algorithm*

51
52
53 Figure 2 illustrates the application of the RT to a realistic video longshore
54 timestack (120×120 pixels, with spatial and temporal resolution of $dx = 0.25$
55 m/pix and $dt = 0.5$ s/pix respectively. Figure 2.a shows the raw image where
56
57
58

1
2
3
4
5
6
7
8
9
10
11
12
13
14
15
16
17
18
19
20
21
22
23
24
25
26
27
28
29
30
31
32
33
34
35
36
37
38
39
40
41
42
43
44
45
46
47
48
49
50
51
52
53
54
55
56
57
58
59
60
61
62
63
64
65

85 both wave crests and drifting foam can be seen. A high-pass radius filter (run-
86 ning average) is applied in the polar space to isolate highly-textured small-scale
87 foam streaks and remove signal longer than a threshold (here $\rho < 20$ points)
88 associated to water background intensity value, remaining foam and long wave
89 crests. Figure 2.b shows the resulting image used to determine the orientation
90 of the current. Figure 2.c shows the RT of the image in Figure 2.a where prop-
91 agating features are clearly visible as local maxima. RT resolution increases for
92 oblique angles around 45° ; it is recommended that the user adapt either spatial
93 or temporal resolution in order not to squeeze signal at 0° or 90° (horizontal
94 or vertical lines). The maximum of variability in the polar domain provides
95 the dominant propagation angle θ (see previous section), which can be further
96 converted into current velocity $V = \tan(\theta)dx/dt$, where dx and dt are spatial
97 and temporal resolution, respectively. V stands for the dominant velocity of the
98 features over the image. Noteworthy, a localized RT or local maxima detection
99 can be applied to retrieve the velocity $V(x, t)$ of individual features.

100 3. Data

101 3.1. Synthetic cases

102 In order to perform a first validation of a current orientation detection algo-
103 rithm, it is possible to simulate synthetic longshore timestacks (Chickadel et al.,
104 2003). The approach proposed in this article is based on anisotropic Gaussian
105 random fields.

106 The Matlab code titled "Generation of Random, Autocorrelated, Periodic
107 Fields" by Cirpka, O.A., available online on <http://m2matlabdb.ma.tum.de> was
108 used to create anisotropic Gaussian random fields. The method utilizes the
109 fact that the Fourier transform of the covariance function is the power spectral
110 density function of all realizations. Random autocorrelated fields are generated
111 by creating random phase spectra meeting the conditions of real numbers in
112 the physical domain. The realizations are then given by back-transformation of
113 the power- and phase-spectrum into the physical domain. Since the method is

1
2
3
4
5
6
7
8
9
10
11
12
13
14
15
16
17
18
19
20
21
22
23
24
25
26
27
28
29
30
31
32
33
34
35
36
37
38
39
40
41
42
43
44
45
46
47
48
49
50
51
52
53
54
55
56
57
58
59
60
61
62
63
64
65

114 based on the discrete Fourier transformation, the generated fields are periodic
115 rather than stationary.

116 The synthetic cases generated for this paper have 100×100 pixels size,
117 Gaussian laws of mean 0 and variance 10. Figures 6.a-c present one synthetic
118 case created with our approach. Figure 6.a shows a first anisotropic Gaussian
119 random field representing the foam pattern. The anisotropy can be compared to
120 an ellipse with a major and minor axes, which are described here by correlation
121 lengths of the signal in x and y , and an orientation θ . If the ratio of correlation
122 lengths decreases, the ellipse is more elongated and the anisotropy increases.
123 The correlation lengths in Figure 6.a are 20 and 2 pixels in x and y , respectively.
124 The orientation is $\theta = 55^\circ$. A second anisotropic Gaussian random field is shown
125 in Figure 6.b representing the incoming waves with correlation lengths in x and
126 y of 50 and 2 pixels, respectively. The orientation of the wave field is $\theta = 0^\circ$.
127 In Figure 6.c, they are combined to obtain a realistic test case.

128 Based on this initial wave-current field, Figures 6.d-f illustrate the influence
129 of the correlation length ratio on the anisotropic Gaussian current fields. The
130 correlation length ratio are 0.05, 0.15 and 0.25. Foam anisotropy decreases when
131 correlation length increases, making streaks angle less evident.

132 To take into account for different levels of drifting streaks signature with
133 waves and lighting conditions, an intensity threshold is applied. In Figures
134 6.f-h, the level of kept information are described by the percentage of pixels
135 not changed, 30%, 50% and 70%, respectively. The lower the percentage of
136 kept information is, the weaker are the foam streaks and more difficult their
137 detection.

138 3.2. Field observations

139 The Bight of Benin(Figure 3) is a sandy open wave-dominated microtidal
140 environment exposed to long period swells (ECMWF Erainterim reanalyse 1979-
141 2013 annual deep water wave averages: $H_s=1.36$ m, $T_p=9.4$ s, Dir= $S - SW$,
142 see Dee (2011)) generated at high latitudes in the South Atlantic. The beach
143 (Figures 2 and 3) presents an longshore-uniform low tide terrace and a steep

1
2
3
4
5
6
7
8
9 144 upper shoreface. An eastward littoral drift of 0.8 to 1.5 m^3/yr has been reported
10 145 in the literature (Anthony & Blivi, 1999; Blivi et al., 2014), driven by year-round
11
12 146 oblique long swells (Almar et al., 2015).

13
14 147 A field experiment was conducted at Grand Popo beach (6.2°N, 1.7°E, Fig-
15 148 ure 3) from 10 to 18 March 2014 (Almar et al., 2014b). Inner shelf waves and
16 149 currents were measured using an Acoustic Doppler Current Profiler (ADCP)
17 150 moored in 10-m depth. Every day, various drifters releases were conducted in
18 151 the surfzone around mid-tide to determine longshore current variability (Castelle
19 152 et al., 2014). An Acoustic Doppler Velocimeter (ADV) was deployed in the
20 153 swash zone during daylight hours. Hourly wind observations are provided by
21 154 Cotonou airport, 80-km distant from Grand Popo and 500 m from the shore
22 155 (i.e. sea breeze is observed). Figure 8 shows that during the experiment, tide
23 156 varied from neap to spring tidal ranges, from 0.3 m to 1.2 m, respectively).
24 157 Waves were energetic and relatively long ($1.2\text{ m} < H_s < 1.6\text{ m}$ and $T_p = 10\text{-}12$
25 158 s), with initial higher waves (up to 1.8 m), coming from south-west, generating
26 159 consistent eastward longshore currents. Surf zone longshore current varied from
27 160 0.4 m/s to 0.8 m/s, inner shelf current from 0.05 to 0.3 m/s, and swash current
28 161 from 0 to 0.5 m/s.

29
30
31 162 A long-term video camera VIVOTEK IP7361, 1600x1200 pixels (Figure 3.c)
32 163 was deployed in February 2013 (Almar et al., 2014b) on a 15 m-high semaphore
33 164 belonging to the navy of the Republic of Benin, 80-m distant from the shore
34 165 (i.e. which is the approximate beach width). During the experiment, full 2-Hz
35 166 videos were stored. Rectification of images from pixels into real world coor-
36 167 dinates was accomplished by direct linear transformation using GPS ground
37 168 control points (Holland et al., 2013) after a correction of the lens radial dis-
38 169 tortion (Heikkila & Silven, 1997) (Figure 3.d). Although varying somewhat
39 170 throughout the field of view, the pixel footprint was less than 0.1 and 0.05 m in
40 171 the region of interest (surf-swash zones of the instrumented zone) for cross-shore
41 172 and longshore direction, respectively (Figure 4). In the video data, the location
42 173 of swash and surf zones were estimated from 10-min averaged cross-shore pixel
43 174 intensity timestacks; the location of the surf being estimated as the maximum
44
45
46
47
48
49
50
51
52
53
54
55
56
57
58
59
60
61
62
63
64
65

1
2
3
4
5
6
7
8
9
10
11
12
13
14
15
16
17
18
19
20
21
22
23
24
25
26
27
28
29
30
31
32
33
34
35
36
37
38
39
40
41
42
43
44
45
46
47
48
49
50
51
52
53
54
55
56
57
58
59
60
61
62
63
64
65

175 of breaking-induced intensity and the swash as the transition between the beach
176 and surf (see illustration in Figure 5). Inner shelf video point is chosen constant,
177 close to the location of the ADCP. For the use of the RT, 100-m long longshore
178 spatio-temporal images (Figure 4) are reinterpolated on a regular grid of 0.25 m
179 and separated into subwindows of 5 m (see sensitivity analyze of the RT on res-
180 olution and windows size in Section 4.2), for resulting sub-images of 20 pixels
181 in space and 120 pixels in time and a regular spatial grid of 5 m both in the
182 cross-shore and longshore directions.

183 [Figure 3 about here.]

184 [Figure 4 about here.]

185 [Figure 5 about here.]

186 [Figure 6 about here.]

187 **4. Results and discussion**

188 *4.1. Tests on synthetic data*

189 A numerical study is performed to determine the sensitivity of the method's
190 skill on the drifting streaks anisotropy, intensity and orientation (i.e. velocity).
191 Numerous synthetic realistic timestacks are generated to cover a wide range of
192 conditions. Figure 7 presents the results of the sensitivity analysis. Figure 7.a
193 shows that method's skills increase with anisotropy (and decrease with correla-
194 tion length ratio) of the Gaussian random current fields. Figure 7.b shows that
195 the threshold value on the current field has not a substantial influence, which
196 indicates that the method is able to detect weak drifting streaks, as encountered
197 offshore of the surf zone. Results in Figure 7.c show that the orientation affects
198 the estimation, with a better accuracy at oblique angles close to 45°.

199 [Figure 7 about here.]

1
2
3
4
5
6
7
8
9
200 *4.2. Comparison with in-situ measurements*

201 Figures 8 and 9 show that video and in-situ currents are in good agreement,
202 with a RMS error of 0.07 m/s (35%, $R^2 = 0.65$, significant at the 95% level).
203 RMS errors are 0.06 m/s (17%), 0.09 m/s (44%) and 0.07 m/s (29%) for the
204 surf, swash and inner shelf zones, respectively. The RT method offers better
205 skills in the surf zone because of clear drifting foam (Figure 4) but is able to
206 estimate the current at more challenging zones where optical signature is weaker:
207 oscillating drift in the swash and turbidity streaks at the inner shelf. These
208 results show the ability of the RT-based method in estimating the whole cross-
209 shore profile of longshore surface current with a better spatial and temporal
210 resolution than any in situ deployment, though accuracy is lower (O(30%)).
211 Figure 10.a shows that the error is linked to the width of the RT peak width
212 in the polar space (correlation coefficient of 0.42, significant at 95% level), the
213 uncertainty increasing with the peak width. This can be used as a proxy to
214 discard estimates with large uncertainties encountered for afternoon sea breeze
215 or sun glint. Figure 10.b shows that the choice of the spatial dimension has
216 only a minor influence. In the contrary, the method accuracy increases with
217 resolution. The resolution might explain part of the errors in the inner shelf,
218 where the pixel footprint worsen to 1-2 m/pixel (Figure 4). Finally, even if
219 the main source of discrepancy can be attributed to the video method itself
220 and geometrical characteristics, in-situ data can cause some spreading in our
221 results, though it is difficult to quantify. Some studies reported accuracy of 0.01
222 to 0.5 m/s (MacMahan et al., 2009) for instant drifter velocities, which is largely
223 reduced by our hourly averaging. The longshore current is considered vertically
224 uniform. However, some discrepancies may arise between video estimate at
225 the surface and in-situ measurements in the water column: 35-cm and 1-m
226 average from the surface for the ADCP and the drifters, respectively, and a few
227 centimeters above the bed for the swash ADV.

228 To illustrate the potential of our method, Figure 11 shows its application
229 to the cross-shore structure of the longshore current. Video-derived profile in
230 Figure 11.a shows a good agreement with in-situ measurements, peaking in the

1
2
3
4
5
6
7
8
9
10
11
12
13
14
15
16
17
18
19
20
21
22
23
24
25
26
27
28
29
30
31
32
33
34
35
36
37
38
39
40
41
42
43
44
45
46
47
48
49
50
51
52
53
54
55
56
57
58
59
60
61
62
63
64
65

231 surf zone and extending to the inner shelf. Swash, surf and inner shelf currents
232 have different behavior. A multiple linear regression with the main forcing
233 (longshore wave energy flux, tide and wind) was conducted over the experiment
234 duration (hourly averaged, when video estimates are available). The relative
235 contribution of each forcing was computed as the ratio of individual variability
236 (variance) over the total reconstructed variance by the multiple liner regression.
237 Figure 8 shows that the swash is dominantly influenced by tidal modulation
238 (40%) of wave action rather than by offshore wave height (30%), certainly due
239 to tidal modulation of surf zone saturation; surf zone is as expected largely
240 dominated by wave action (65%) and wind dominates (20%) at the inner shelf.
241 The decrease of the total reconstructed signal with the distance to the shore
242 (from 90 % in the surf to 25 % on the shelf) denotes the difficulties in retrieving
243 the surface current with decreasing pixel resolution and less drifting features,
244 but also suggests a complex transitional zone behavior, influenced by both inner
245 shelf and nearshore processes. This difference of forcing for the three zones has
246 considerable implications in terms of longshore sediment drift. The possibility
247 of using the RT to estimate longshore current clearly provides new perspectives
248 in quantifying the longshore sediment drift and its variability.

249 [Figure 8 about here.]

250 [Figure 9 about here.]

251 [Figure 10 about here.]

252 [Figure 11 about here.]

253 **5. Conclusions**

254 Our understanding of the nearshore longshore current has been hampered
255 for long by the lack of adapted tool. This article presents a new approach to
256 estimate longshore currents from video spatio-temporal fields using the Radon
257 transform, recently applied to waves (Almar et al., 2014a). It is an alternative

1
2
3
4
5
6
7
8
9
10
11
12
13
14
15
16
17
18
19
20
21
22
23
24
25
26
27
28
29
30
31
32
33
34
35
36
37
38
39
40
41
42
43
44
45
46
47
48
49
50
51
52
53
54
55
56
57
58
59
60
61
62
63
64
65

258 to other approaches in one (Chickadel et al., 2003) and two dimensions (Holland
259 et al., 2001). The Radon transform is tested and validated on synthetic and field
260 data collected during the Grand Popo 2014 (Benin, West Africa) experiment.
261 A sensitivity analyze using synthetic data shows that method’s skills improve
262 with streaks anisotropy and for oblique orientation close to 45° but stays fairly
263 insensitive to the level of streaks signature. Comparison with field data shows
264 a good agreement ($O(30\%)$) in the swash, surf and inner shelf zones with RMS
265 errors of 0.06 m/s (17%), 0.09 m/s (44%) and 0.07 m/s (29%), respectively.
266 Error worsen when resolution decreases and Radon transform polar density peak
267 enlarges. A first application of this method shows that during the experiment,
268 swash, surf and inner shelf longshore currents were controlled preferentially
269 by tide, waves and wind, respectively. This clearly illustrates the potential of
270 such remote method in quantifying the longshore current, in particular when
271 considering its spatio-temporal variability and the need to cover longer scales.

272 **6. Acknowledgments**

273 This study was funded by the French grants through ANR (COASTVAR:
274 ANR-14-ASTR-0019) and INSU (LEFE and EC2CO programs), and the UN-
275 ESCO co-chair ICPMA/IRHOB. We are greatly indebted to the naval services of
276 Benin at Grand Popo for their logistic support during the field experiment and
277 for allowing the installation of the permanent video system on the semaphore.

278 **References**

279 Allen, J., Newberger, P., & Holman, R. (1996). The grand popo experiment,
280 benin. *Journal of Fluid Mechanics*, 310.

281 Almar, R., Bonneton, P., Michallet, H., Cienfuegos, R., Ruessink, B., & Tissier,
282 M. (2014a). On the use of radon transform in studying nearshore wave dy-
283 namics. *Coastal Engineering*, 92, 24-30.

1
2
3
4
5
6
7
8
9
10
11
12
13
14
15
16
17
18
19
20
21
22
23
24
25
26
27
28
29
30
31
32
33
34
35
36
37
38
39
40
41
42
43
44
45
46
47
48
49
50
51
52
53
54
55
56
57
58
59
60
61
62
63
64
65

284 Almar, R., Cienfuegos, R., Cataln, P., Michallet, H., Castelle, B., Bonneton,
285 P., & Marieu, V. (2012). A new breaking wave height direct estimator from
286 video imagery. *Coastal Engineering*, 61, 24–30.

287 Almar, R., Du Penhoat, N., Y.and Honkonnou, Castelle, B., Laibi, R., Anthony,
288 E., N., S., Degbe, G., Chuchla, R., Sohoul, Z., & Dorel, M. (2014b). The grand
289 popo experiment, benin. *Journal of Coastal Research*, SI 70, 651–656.

290 Almar, R., Kestenare, E., Reyns, J., Jouanno, J., Anthony, E., Laibi, R., Hemer,
291 M., Du Penhoat, Y., & Ranasinghe, R. (2015). Response of the gulf of guinea
292 coastline to anthropogenic and natural forcing, part1: Wave climate variabil-
293 ity and impacts on longshore sediment transport. *Continental Shelf Research*,
294 110, 48–59.

295 Anthony, E., & Blivi, A. (1999). Morphosedimentary evolution of a delta-
296 sourced, drift-aligned sand barrier-lagoon complex, western bight of benin.
297 *Marine Geology*, 158, 161–176.

298 Blivi, A., Anthony, E., & Oyd, L.-M. (2014). Sand barrier development in the
299 bight of benin, west africa. *Ocean and Coastal Management*, 45, 185–200.

300 Castelle, B., du Penhoat, Y., Almar, R., Anthony, E., Lefebvre, J., Laibi, R.,
301 Chuchla, R., Dorel, M., & Senechal, N. (2014). Flash rip dynamics on a high-
302 energy low-tide-terraced beach (grand popo, benin, west africa). *Journal of*
303 *Coastal Research*, SI 70, 633–638.

304 Chickadel, C., Holman, R., & Freilich (2003). An optical technique for the
305 measurement of longshore currents. *J. Geophys. Research: Oceans*, 108(C11),
306 73–82.

307 Copeland, A., Ravichandran, G., & Trivedi, M. (1995). Localized radon
308 transform-based detection of ship wakes in sar images. *IEEE Transactions of*
309 *Geoscience and Remote Sciences*, 33, 35–45.

310 Cox, D., & Anderson, S. (2001). Statistics of intermittent surf zone turbulence
311 and observations of large eddies using piv. *Coastal Engineering*, 43, 121–131.

- 1
2
3
4
5
6
7
8
9
10
11
12
13
14
15
16
17
18
19
20
21
22
23
24
25
26
27
28
29
30
31
32
33
34
35
36
37
38
39
40
41
42
43
44
45
46
47
48
49
50
51
52
53
54
55
56
57
58
59
60
61
62
63
64
65
- 312 De Vries, S., Hill, D., De Schipper, M., & Stive, M. (2011). Remote sensing of
313 surf zone waves using stereo imaging. *Coastal Engineering*, *58*(3), 239–250.
- 314 Dee, D. e. a. (2011). The era-interim reanalysis: configuration and performance
315 of the data assimilation system. *Q. J. R. Meteorol. Soc.*, *137*, 553597.
- 316 Feddersen, F. (2003). Observations of nearshore circulation: Alongshore unifor-
317 mity. *J. Phys. Oceanogr.*, *108*, DOI: 10.1029/2001JC001293.
- 318 Feddersen, F. (2014). The generation of surfzone eddies in a strong alongshore
319 current. *J. Phys. Oceanogr.*, .
- 320 Feeman, T. G. (2010). The mathematics of medical imaging, a beginner’s guide.
321 *Springer Undergraduate Texts in Mathematics and Technology*. Springer, New
322 York, .
- 323 Haller, R., M.C. Dalrymple, & Svendsen, I. (2002). Experimental study of
324 nearshore dynamics on a barred beach with rip channels. *J. Geophys. Res.*,
325 *107*, 3061.
- 326 Haller, R., M.C. Dalrymple, & Svendsen, I. (2014). Rip current observations via
327 marine radar. *J. Waterway, Port, Coastal, and Ocean Engineering*, *140*(2),
328 115–124.
- 329 Heikkila, J., & Silven, O. (1997). A four-step camera calibration procedure
330 with implicit image correction. *Computer Vision and Pattern Recognition*. In
331 *Proceedings of the IEEE Computer Society Conference*, (pp. 1106–11012).
- 332 Holland, K., Holman, R., Lippmann, T., Stanley, J., & Plant, N. (2013). Prac-
333 tical use of video imagery in nearshore oceanographic field studies. *Oceanic
334 Engineering*, *22*(1), 81–82.
- 335 Holland, K., Puleo, J., & Kooney, T. (2001). Quantification of swash flows using
336 video-based particle image velocimetry. *Coast. Eng.*, *44*(2), 6577.
- 337 Holman, R., & Haller, M. (2013). Remote sensing of the nearshore. *Annual
338 Review of Marine Science*, *113*, 5–95.

- 1
2
3
4
5
6
7
8
9 339 Kimmoun, O., & Branger, H. (2007). A particle images velocimetry investigation
10 on laboratory surf-zone breaking waves over a sloping beach. *Journal of Fluid*
11 *Mechanics*, 588, 353–397.
12
13
14 342 Komar, P. (1998). Beach processes and sedimentation. *2nd edition, Prentice-*
15 *Hall, NJ*, (p. 544 p).
16
17
18 344 Komar, P., & Inman, D. L. (1970). Longshore sand transport on beaches. *J.*
19 *Geophys. Res.*, 75(30), 5914–5927.
20
21
22 346 Lippmann, T. (1970). Longshore currents generated byobliquely incident sea
23 waves. *J. Geophys. Res.*, 75, 6778–6789.
24
25
26 348 Lippmann, T., & Holman, R. (1990). The spatial and temporal variability of
27 sand bar morphology. *J. Geophys. Research: Oceans*, 95(C7), 11575–11590.
28
29
30 350 Lippmann, T., & Holman, R. (1991). Phase speed and angle of breaking waves
31 measured with video techniques. In N.C. Kraus, K.J. Gingerich, and D.L.
32 Kriebel, editors, *Coastal Sediments, SI 70*, 542–556.
33
34
35 353 MacMahan, J., Brown, J., & Thornton, E. (2009). Low-cost hand-held global
36 positioning system for measuring surfzone currents. *Journal of Coastal Re-*
37 *search*, 25(3), 744–754.
38
39
40 356 Mallat, S. (2008). *A Wavelet Tour of Signal Processing, Third Edition: The*
41 *Sparse Way*. (3rd ed.). Academic Press.
42
43
44 358 Mole, M., Mortlock, T., Turner, I., Goodwin, I., Splinter, K., & Short, A.
45 (2013). Capitalizing on the surfcam phenomenon: a pilot study in regional-
46 scale shoreline and inshore wave monitoring utilizing existing camera infras-
47 tructure. *J. Coast. Res.*, 65, 6778–6789.
48
49
50
51 362 Oltman-Shay, J., Howd, P., & Birkemeier, W. (1989). Shear instabilities of the
52 mean longshore current: 2. field observations. *J. Geophys. Res.*, 94, 18031–
53 18042.
54
55
56
57
58
59
60
61
62
63
64
65

- 1
2
3
4
5
6
7
8
9 365 Plant, N., & Holman, R. (1997). Intertidal beach profile estimation using video
10 366 images. *Mar. Geol.*, *140*, 124.
- 11
12 367 Puloe, J., Farquharson, G., Frasier, S., & Holland, K. (2003). Comparison of
13 368 optical and radar measurements of surf and swash zone velocity fields. *J.*
14 369 *Geophysical Res.*, *108*, C3 3100.
- 15
16
17
18 370 Putrevu, J., U. Oltman-Shay, & Svendsen, I. (1995). Intertidal beach profile
19 371 estimation using video images. *J. Geophysical Res.*, *100*, 16119–16130.
- 20
21
22 372 Radon, J. (1917). Uber die bestimmung von funktionen durch ihre integralwerte
23 373 l'angs gewisser mannigfaltigkeiten. *Akad. Wiss.*, *69*, 262–277.
- 24
25
26 374 Ramm, A., & Katsevich, A. (1996). *The Radon Transform and Local Tomogra-*
27 375 *phy*. Taylor & Francis.
- 28
29
30 376 Schoonees, J., & Theron, A. (1993). Review of the field database for longshore
31 377 sediment transport. *Coastal Engineering*, *19*, 1–25.
- 32
33
34 378 Splinter, K., Davidson, M., Golshani, A., & Tomlinson, R. (2012). Climate
35 379 controls on longshore sediment transport. *Continental Shelf Research*, *48*,
36 380 146–156.
- 37
38
39 381 Stockdon, H. F., & Holman, R. (2000). Estimation of wave phase speed and
40 382 nearshore bathymetry from video imagery. *Journal of Geophysical Research*
41 383 *- Oceans*, *105*, null+. URL: <http://dx.doi.org/10.1029/1999jc000124>.
- 42
43
44 384 Thornton, E., & Guza, R. (1986). Surf zone longshore currents and random
45 385 waves: Field data and models. *J. Phys. Oceanogr.*, *16*, 1165–1178.
- 46
47
48 386 Yoo, J., Fritz, H., Haas, K., Work, P., & Barnes, C. (2009). Waves swash
49 387 velocity estimation using ridgelet transform. *In: 9th Int. Conf. Electronic*
50 388 *Meas. and Instr. ICEMI 09*, (pp. 1078–1081).
- 51
52
53 389 Yoo, J., Fritz, H., Haas, K., Work, P., & Barnes, C. (2011). Depth inversion in
54 390 the surf zone with inclusion of waves non-linearity using video-derived celerity.
55 391 *J. Waterw. Port Coastal Oc. Eng.*, *137(2)*, 95–106.

392 **List of Figures**

393	1	Radon transform (RT) practical use. RT of a disk and inclined lines in upper and lower panels respectively, and from left to right: original fields, RT in polar space, and resulting integrated angular density.	18
394			
395			
396			
397	2	Illustration on the separation of waves from drifting features in longshore spatio-temporal images using the RT. a) mixed wave-current intensity timestack, b) wave-filtered current timestack and c) Polar space visualization of timestack in b). Grand Popo spatio-temporal longshore image from video, $dx = 0.25m/pix$, $dt = 0.5s$. Dashed line at $\theta = 106^\circ$ shows the variance maximum, or dominant velocity ($V = 0.14m/s$).	19
398			
399			
400			
401			
402			
403			
404	3	Grand Popo beach (6.2°N, 1.7°E), in the Bight of Benin, Gulf of Guinea West Africa (a-b). c) Permanent video camera, on a 15-m high semaphore and d) rectified 15-min averaged image from video system.	20
405			
406			
407			
408	4	Instant video image with superimposed black iso-contours of pixel footprint (m/pix) in the longshore direction and in white location of 100-m long longshore spatio-temporal transects, b) in the swash, c) surf and d) inner shelf zones. Drifting features at these 3 zones are clearly visible.	21
409			
410			
411			
412			
413	5	Cross-shore timestack derived from time-averaged images. Time-varying swash and surfzone locations used in the RT method are superimposed. Inner shelf location is taken constant.	22
414			
415			
416	6	Examples of synthetic test cases, a-c): from left to right, anisotropic random Gaussian currents and wave fields and a combination of both. Random Gaussian current field with in d-f) from left to right, correlation ratio of 0.05, 0.15 and 0.25, and in g-i) from left to right, thresholds on kept pixels of 30%, 50% and 70%.	23
417			
418			
419			
420			
421	7	Sensitivity analyze on RT skills in retrieving current velocity from synthetic Gaussian random current fields. RMSE error as a function of a) Correlation length ratio (isotropy), b) threshold on kept information (in percent of pixels not changed) and c) orientation (or velocity).	24
422			
423			
424			
425			
426	8	Forcing and longshore current during Grand Popo 2014 experiment. a) Waves (H_s , T , Dir) and b) tide measured by ADCP, c) observed wind at Cotonou airport d) Comparison of co-localized video (continuous line) and in-situ current measurements in the surf zone (red), swash (black) and inner shelf (blue), from drifters, ADV and ADCP, respectively.	25
427			
428			
429			
430			
431			
432	9	Video-derived versus in-situ current, in the surf zone (red), swash (black) and inner shelf (blue), from drifters, ADCP and ADV, respectively.	26
433			
434			

1
2
3
4
5
6
7
8
9
10
11
12
13
14
15
16
17
18
19
20
21
22
23
24
25
26
27
28
29
30
31
32
33
34
35
36
37
38
39
40
41
42
43
44
45
46
47
48
49
50
51
52
53
54
55
56
57
58
59
60
61
62
63
64
65

435	10	RT-method error as a function of a) RT-transform peakness (width	
436		of the peak in polar space) and b) resolution (0.1 m/pixel (triangles),	
437		0.2 m/pixel (circles) and 0.4 m/pixel (squares)) and spatial	
438		dimension (pixels). In a) are shown estimates for the inner shelf	
439		(blue), surf- (red) and swash-zones (black).	27
440	11	a) Cross-shore profile of longshore current derived from the RT	
441		(continuous line), ADV in the swash (square), drifters in the surf	
442		(circle) and ADCP (diamond), averaged when both video and	
443		in-situ measurements were available. b) Percentage of variance	
444		of RT-derived current timeseries at each location retrieved from	
445		waves and tide (ADCP) and wind (80-km distant Cotonou airport	
446		- 500 m from coastline).	28

1
2
3
4
5
6
7
8
9
10
11
12
13
14
15
16
17
18
19
20
21
22
23
24
25
26
27
28
29
30
31
32
33
34
35
36
37
38
39
40
41
42
43
44
45
46
47
48
49
50
51
52
53
54
55
56
57
58
59
60
61
62
63
64
65

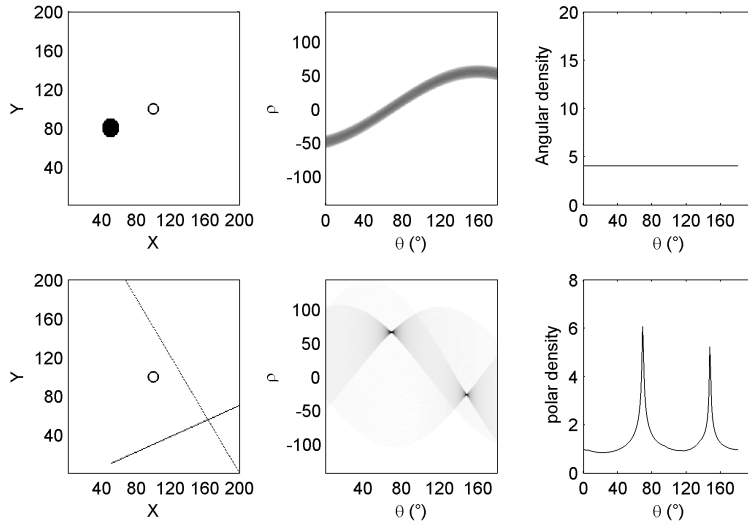


Figure 1: Radon transform (RT) practical use. RT of a disk and inclined lines in upper and lower panels respectively, and from left to right: original fields, RT in polar space, and resulting integrated angular density.

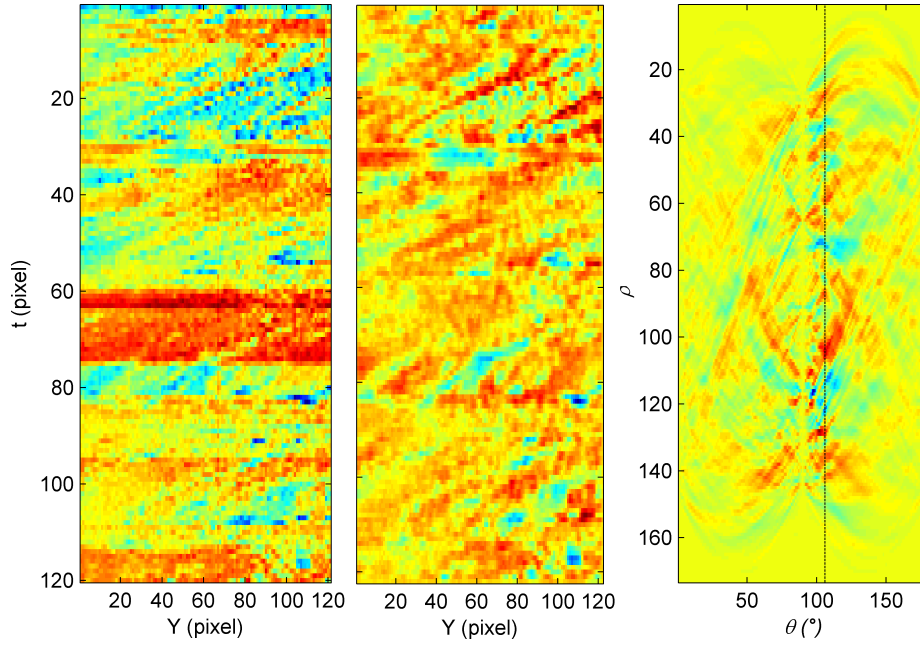


Figure 2: Illustration on the separation of waves from drifting features in longshore spatio-temporal images using the RT. a) mixed wave-current intensity timestack, b) wave-filtered current timestack and c) Polar space visualization of timestack in b). Grand Popo spatio-temporal longshore image from video, $dx = 0.25m/pix$, $dt = 0.5s$. Dashed line at $\theta = 106^\circ$ shows the variance maximum, or dominant velocity ($V = 0.14m/s$).

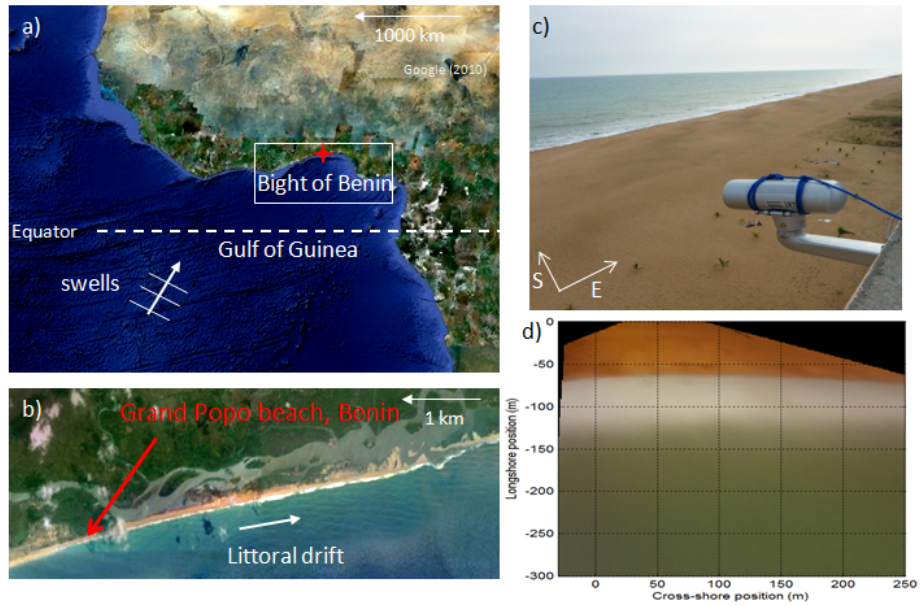


Figure 3: Grand Popo beach (6.2°N , 1.7°E), in the Bight of Benin, Gulf of Guinea West Africa (a-b). c) Permanent video camera, on a 15-m high semaphore and d) rectified 15-min averaged image from video system.

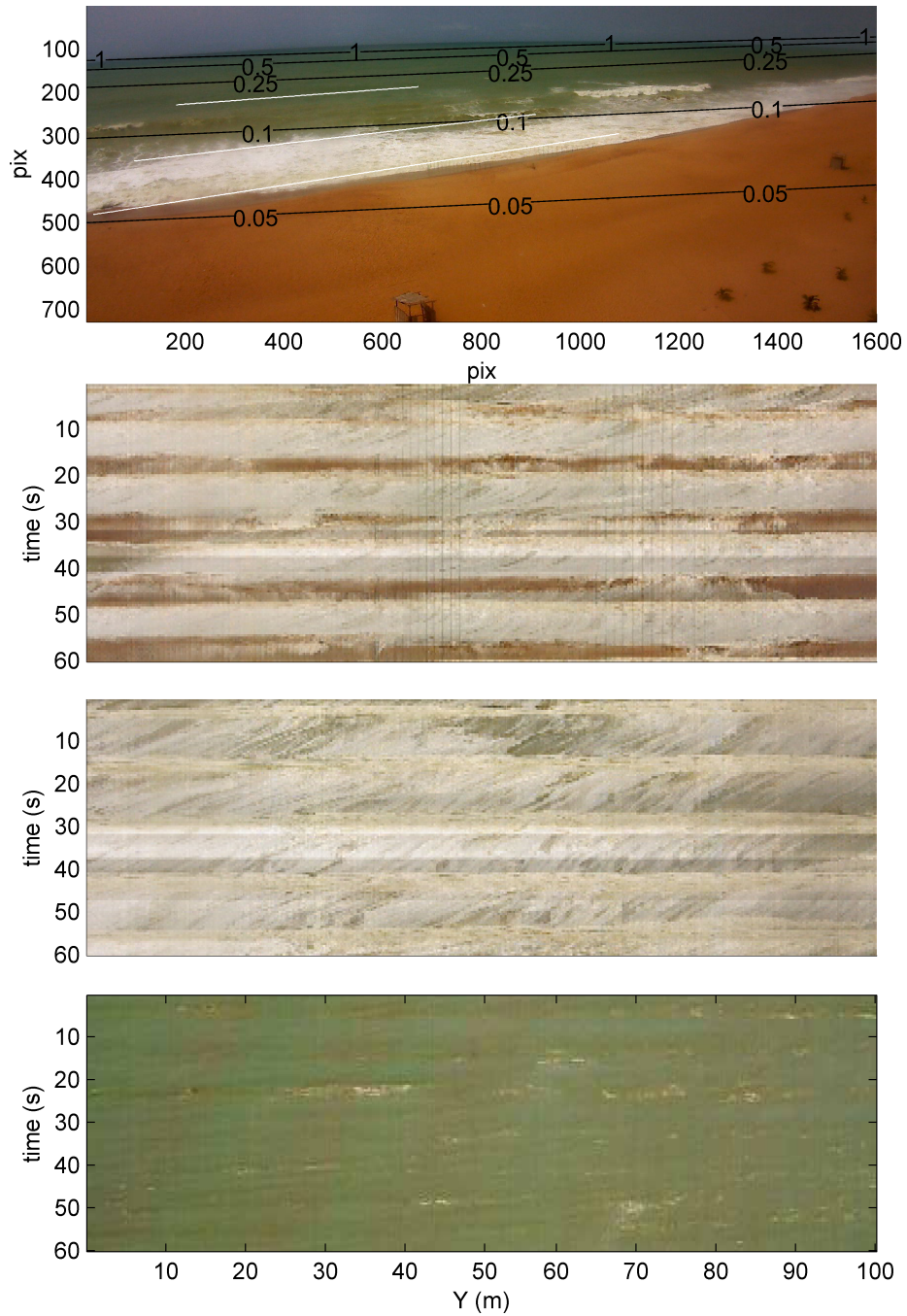


Figure 4: Instant video image with superimposed black iso-contours of pixel footprint (m/pix) in the longshore direction and in white location of 100-m long longshore spatio-temporal transects, b) in the swash, c) surf and d) inner shelf zones. Drifting features at these 3 zones are clearly visible.

1
2
3
4
5
6
7
8
9
10
11
12
13
14
15
16
17
18
19
20
21
22
23
24
25
26
27
28
29
30
31
32
33
34
35
36
37
38
39
40
41
42
43
44
45
46
47
48
49
50
51
52
53
54
55
56
57
58
59
60
61
62
63
64
65

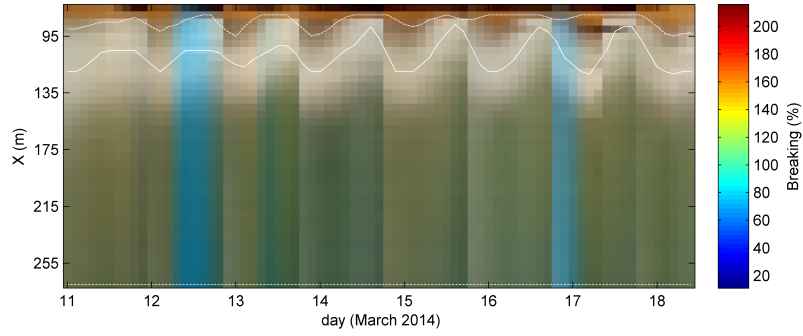


Figure 5: Cross-shore timestack derived from time-averaged images. Time-varying swash and surfzone locations used in the RT method are superimposed. Inner shelf location is taken constant.

1
2
3
4
5
6
7
8
9
10
11
12
13
14
15
16
17
18
19
20
21
22
23
24
25
26
27
28
29
30
31
32
33
34
35
36
37
38
39
40
41
42
43
44
45
46
47
48
49
50
51
52
53
54
55
56
57
58
59
60
61
62
63
64
65

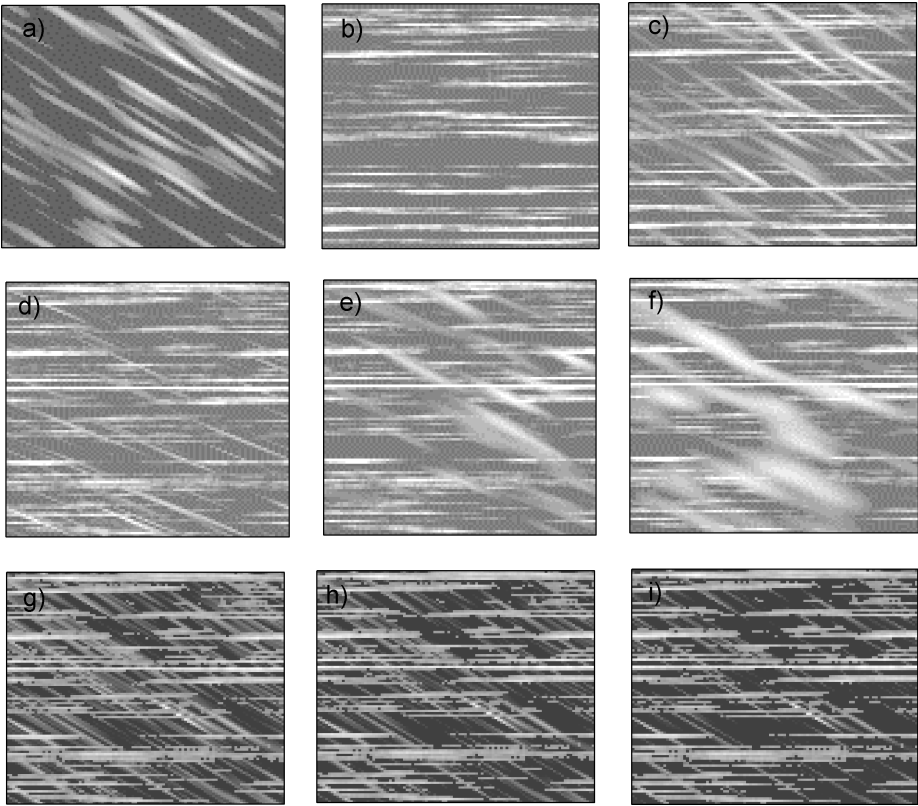


Figure 6: Examples of synthetic test cases, a-c): from left to right, anisotropic random Gaussian currents and wave fields and a combination of both. Random Gaussian current field with in d-f) from left to right, correlation ratio of 0.05, 0.15 and 0.25, and in g-i) from left to right, thresholds on kept pixels of 30%, 50% and 70%.

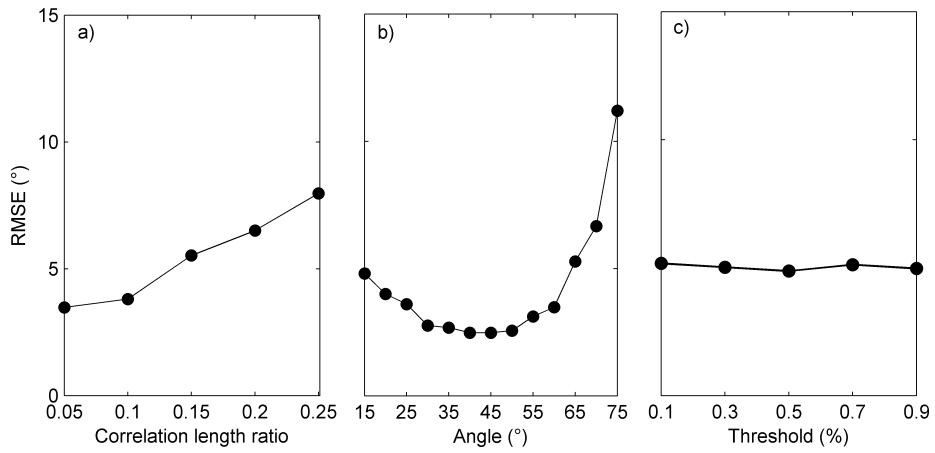


Figure 7: Sensitivity analyze on RT skills in retrieving current velocity from synthetic Gaussian random current fields. RMSE error as a function of a) Correlation length ratio (isotropy), b) threshold on kept information (in percent of pixels not changed) and c) orientation (or velocity).

1
2
3
4
5
6
7
8
9
10
11
12
13
14
15
16
17
18
19
20
21
22
23
24
25
26
27
28
29
30
31
32
33
34
35
36
37
38
39
40
41
42
43
44
45
46
47
48
49
50
51
52
53
54
55
56
57
58
59
60
61
62
63
64
65

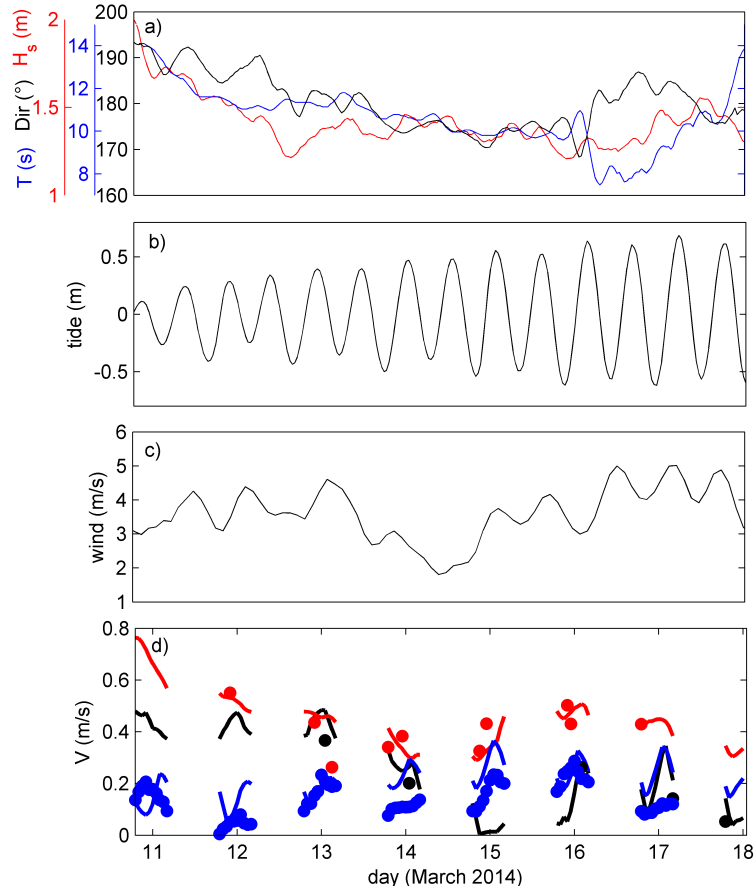


Figure 8: Forcing and longshore current during Grand Popo 2014 experiment. a) Waves (H_s , T , Dir) and b) tide measured by ADCP, c) observed wind at Cotonou airport d) Comparison of co-localized video (continuous line) and in-situ current measurements in the surf zone (red), swash (black) and inner shelf (blue), from drifters, ADV and ADCP, respectively.

1
2
3
4
5
6
7
8
9
10
11
12
13
14
15
16
17
18
19
20
21
22
23
24
25
26
27
28
29
30
31
32
33
34
35
36
37
38
39
40
41
42
43
44
45
46
47
48
49
50
51
52
53
54
55
56
57
58
59
60
61
62
63
64
65

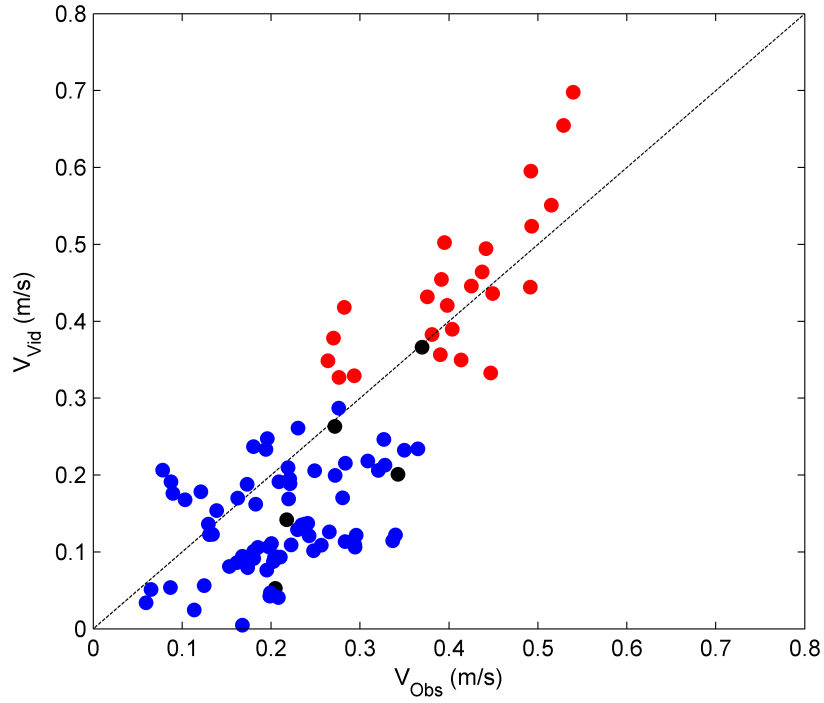


Figure 9: Video-derived versus in-situ current, in the surf zone (red), swash (black) and inner shelf (blue), from drifters, ADCP and ADV, respectively.

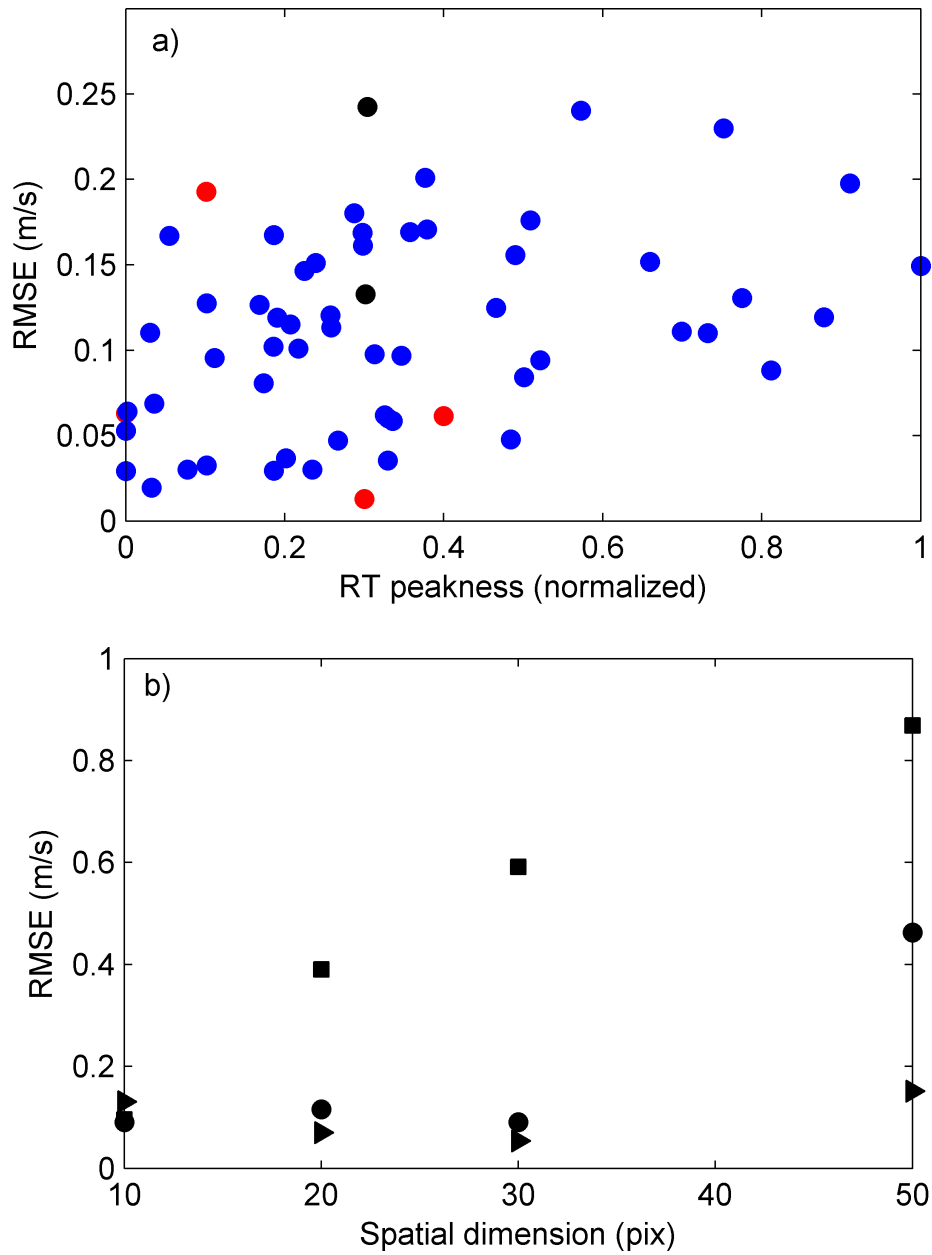


Figure 10: RT-method error as a function of a) RT-transform peakness (width of the peak in polar space) and b) resolution (0.1 m/pixel (triangles), 0.2 m/pixel (circles) and 0.4 m/pixel (squares)) and spatial dimension (pixels). In a) are shown estimates for the inner shelf (blue), surf- (red) and swash-zones (black).

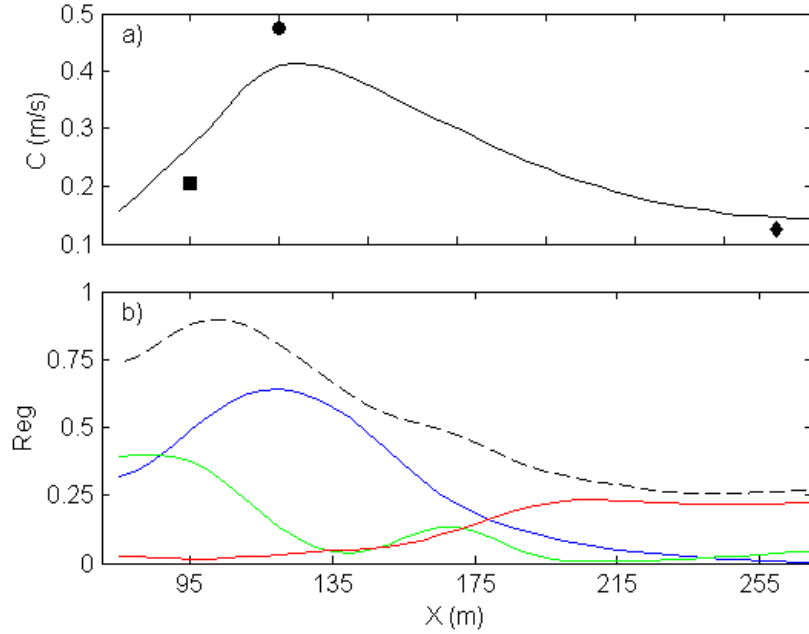


Figure 11: a) Cross-shore profile of longshore current derived from the RT (continuous line), ADV in the swash (square), drifters in the surf (circle) and ADCP (diamond), averaged when both video and in-situ measurements were available. b) Percentage of variance of RT-derived current timeseries at each location retrieved from waves and tide (ADCP) and wind (80-km distant Cotonou airport - 500 m from coastline).